In the format provided by the authors and unedited.

Earth's multi-scale topographic response to global mantle flow

D. R. Davies [1]*, **A. P. Valentine** [1], **S. C. Kramer**[2], **N. Rawlinson** [3], **M. J. Hoggard** [4], **C. M. Eakin**[1] **and C. R. Wilson**[5]

[1]Research School of Earth Sciences, The Australian National University, Canberra, Australia. [2]Department of Earth Science and Engineering, Imperial College London, London, UK. [3]Department of Earth Sciences-Bullard Labs, University of Cambridge, Cambridge, UK. [4]Department of Earth and Planetary Sciences, Harvard University, Cambridge, MA, USA. [5]Department of Terrestrial Magnetism, Carnegie Institution of Washington, Washington, DC, USA. *e-mail: rhodri.davies@anu.edu.au

Supplementary Information:
Earth's Multi-scale Topographic Response to Global Mantle Flow

D.R. Davies[1], A.P. Valentine[1], S.C. Kramer[2], N. Rawlinson[3], M.J. Hoggard[4], C.M. Eakin[1], and C.R. Wilson[5]

[1]Research School of Earth Sciences, The Australian National University, Canberra, Australia.
[2]Department of Earth Science and Engineering, Imperial College London, UK.
[3]Department of Earth Sciences-Bullard Labs, University of Cambridge, Cambridge, UK.
[4]Department of Earth and Planetary Sciences, Harvard University, MA, USA.
[5]Department of Terrestrial Magnetism, Carnegie Institution of Washington, Washington, DC, USA.

Residual Topography Dataset: Observational constraints on the spatial pattern, wavelength and amplitude of residual topography are central to this study. We utilise an updated compilation of residual topography measurements, based upon the database and methodology of Hoggard *et al.* (2017) [1], which builds on a number of previous regional studies [2, 3, 4]. In comparison to [1], existing marine seismic experiments have been further quality checked and supplemented with additional surveys. The final database contains 1,328 reflection profiles, 305 modern wide-angle experiments and 394 vintage seismic refraction experiments. This provides point-wise coverage of the oceanic realm, with points concentrated at thickly sedimented continental margins. At each location, careful analyses were undertaken to remove the isostatic consequences of variable sedimentary loading, and also crustal thickness where possible. Age-depth cooling is removed using a simple analytical plate model [1]. This differs from [5] who used the empirical age-depth relationship of Crosby *et al.* (2009) [6]. We use an updated oceanic age-grid [7] that is largely based upon the age grid of [8], but corrects gridding artefacts and includes additional missing sites of oceanic lithosphere. Finally, we remove any measurement that does not include a crustal correction if it occurs within 111 km of a measurement that does. Our updated database comprises 2,030 spot measurements, including 1,160 highly-accurate points that incorporate a crustal correction (circles in Supplementary Fig. 1a) and 870 that do not (triangles). To account for the lack of a crustal correction, an additional 0.2 km of uncertainty has been added to triangles, in accordance with the typical magnitude of the crustal correction.

To provide more comprehensive coverage across the oceanic realm, this dataset has been supplemented by ship-track residual depth estimates compiled using the same approach [1]. Water depth is measured from ship-track bathymetry [9] and sedimentary corrections are calculated using global digital grids [10]. Sedimentary corrections are particularly uncertain along continental margins and, accordingly, regions where sediment thickness exceeds 1.5 km were excised, as well as areas with anomalously thick or thin crust, including seamounts, plateaus and fracture zones. Furthermore, the lack of global grids of oceanic crustal thickness prevents application of a crustal correction. Thus, we have also added 0.2 km uncertainty to ship-track based estimates. We note that, at their intersections, ship-track derived estimates

generally match the point-wise measurements [5, 1] (Supplementary Fig. 1b).

On continents, attempts to constrain residual topography are complicated by variable lithospheric architecture and structural complexity [11]. Nonetheless, in an attempt to better constrain a global spherical harmonic residual topography model, Hoggard *et al.* (2016) [5] further supplemented this dataset with a series of continental models. Their main model assumed a constant admittance to transform free-air gravity anomalies to residual topography (Supplementary Fig. 1c). Several studies have since demonstrated, however, that free-air gravity anomalies cannot robustly constrain dynamic topography: the assumption of constant admittance is therefore invalid, with potential for large dynamic topography without large free-air gravity anomalies [12, 13, 14]. Accordingly, in this study, we utilise residual topography estimates (point-wise/spot and ship-track) from the oceanic realm only.

Power Spectral Decompositions using a Tikhonov-style regularisation Approach: Here, we explore the consequences of utilising the Tikhonov-style regularisation approach, as in Hoggard *et al.* (2016) [5]. In [5], the regularisation operator was constructed to prefer low-amplitude, smooth solutions, consistent with the principle of 'Occam's Razor'. We remark that 'smooth' can be defined in different ways; [5] chose to penalise the first derivative of the recovered field, and the total power contained within it (i.e. the sum of squares of model coefficients). The relative weights assigned to each penalty term were governed by two tuneable parameters, which we denote by α (overall power term) and β (gradient term). [5] explored regularisation parameter values, adopting $\alpha = 20$ and $\beta = 1$ for their core results, with ranges of 10–32 and 0.56–1.78, respectively (using definitions from this paper). This choice was motivated by inspection of the trade-off curve (L-curve) for misfit against parameters. To simplify the process of comparing results across different simulations, we adopt an automatic regularisation parameter selection algorithm, as described in [15]. This employs a hierarchical Bayesian approach, designed to ensure that the regularisation is statistically consistent with the observational constraints. Applying this to our oceanic point-wise and ship-track residual topography dataset, we determine optimal values of $\alpha = 1.25$ and $\beta = 1.28$. We use this regularisation and perform several inversions: two for each of our simulations, the first with full global coverage and the second sampled only at the (spot & ship-track) data point locations, with a further inversion using the observational constraints. In all cases, we invert for a model up to maximum spherical harmonic degree $l_{\max} = 50$, but plot results only up to $l = 30$. In doing so, we aim to minimise effects arising from spectral leakage [16].

Results of these inversions are shown in Supplementary Fig. 3(a); we use solid lines to denote inversion of full data, and dotted lines for inversion of sampled data. The difference in spectral characteristics between the two simulations is clear: whether full or sampled datasets are used, the simulation with shallow structure shows a relatively flat spectrum, similar to that preferred by [5], while the simulation without shallow structure has a rapid drop-off in power beyond the lowest degrees. These trends are consistent with the unregularised power spectra illustrated in Fig. 1(f) of the main manuscript. When all simulation data is used (i.e. full global coverage), these results are extremely well-constrained, such that there is minimal uncertainty on the power spectra; however, once the data is sampled to correspond to available observational constraints, this is no longer the case. Within the Bayesian interpretation, we obtain Gaussian

2

uncertainties on the recovered model coefficients. However, since the power spectrum depends on the square of these coefficients, spectral uncertainties are non-Gaussian. To provide an intuitive understanding of the range of spectra that could be compatible with data, Supplementary Fig. 3(a) also includes ranges that can be interpreted as 50% and 99% confidence intervals on the spectra obtained using realistically-sampled data. Looking at results from inversion of simulations lacking shallow structure especially, we see a counter-intuitive effect that emerges from the non-Gaussian statistics: the spectrum of the most-probable model (i.e. the red dotted line) lies well outside even the 99% confidence interval. Although this synthetic dataset is known to have very little power at high degrees, most fields that can be constructed to match data and our prior assumptions will over-estimate the power by up to two orders of magnitude, beyond $l = 5$. Thus, consistent with [14, 17], based upon these analyses, we would suggest that above $l \approx 5$ it is difficult to argue that the results of [5] falsify arguments from the predictive modelling community.

Of course, these spectra are dependent on the values of α and β estimated from the observational constraints. In Supplementary Figs. 3(b) and 3(c), we show examples where α and β are instead determined from one or other of the simulated datasets. When the simulation without shallow structure is used (Supplementary Fig. 3b), results are distinct from those of Supplementary Fig. 3(a), but the spectrum of the simulated data remains of a different character to that derived from the observational constraints. On the other hand, when the simulation containing shallow structure is used to determine the regularisation parameters, synthetic predictions and observational constraints are relatively similar. Given the framing of the determination procedure, this suggests that the observational constraints have characteristics that are more similar to those of the simulation with shallow structure, than the one without. For completeness, in Supplementary Fig. 4, we illustrate results from comparable inversions using only the 2,030 spot measurements: these are generally consistent with those obtained when both the spot and ship-track locations are used.

Nevertheless, these results are predicated upon the assumptions implicit within the form of regularisation operator introduced by [5]. As highlighted in the main manuscript, these express a prior preference for a relatively flat power spectrum (Supplementary Fig. 2), making it difficult to assess whether the results of [5] reflect signal in the data, or simply the initial biases. Our study overcomes this shortcoming using a different style of regularisation, termed Automatic Relevance Determination (ARD) [18, 15]. Unfortunately, it is difficult to apply the ARD approach to the spot measurements alone, as there is insufficient data to robustly estimate appropriate hyperparameters (noting that 50 hyperparameters would need to be determined from only 2,030 spot measurements).

References

[1] Hoggard, M. J., Winterbourne, J., Czarnota, K. & White, N. Oceanic residual depth measurements, the plate cooling model, and global dynamic topography. *J. Geophys. Res.* **122**, 2328–2372 (2017).

[2] Winterbourne, J. R., Crosby, A. G. & White, N. J. Depth, age and dynamic topography of oceanic lithosphere beneath heavily sedimented atlantic margins. *Earth Planet. Sci. Lett.* **287**, 137–151 (2009).

[3] Czarnota, K., Hoggard, M. J., White, N. & Winterbourne, J. Spatial and temporal patterns of Cenozoic dynamic topography around Australia. *Geochem. Geophys. Geosys.* **14**, 634–658 (2013).

[4] Winterbourne, J. R., White, N. J. & Crosby, A. G. Accurate measurements of residual topography from the oceanic realm. *Tectonics* **33**, 1–34 (2014).

[5] Hoggard, M. J., White, N. & Al-Attar, D. Global dynamic topography observations reveal limited influence of large-scale mantle flow. *Nat. Geo.* **9**, 456–463 (2016).

[6] Crosby, A. G. & McKenzie, D. An analysis of young ocean depth, gravity and global residual topography. *Geophys. J. Int.* **178**, 1198–1219 (2009).

[7] Richards, F. D., Hoggard, M. J., Cowton, L. R. & White, N. J. Reassessing the thermal structure of oceanic lithosphere with revised global inventories of basement depths and heat flow measurements. *J. Geophys. Res.* **123**, 9136–9161 (2018).

[8] Muller, R. D. *et al.* Ocean Basin Evolution and Global-Scale Plate Reorganization Events Since Pangea Breakup. *Ann. Rev. Earth Planet. Sci.* **44**, 107–138 (2016).

[9] Smith, W. H. F. & Sandwell, D. T. Global sea floor topography from satellite altimetry and ship depth soundings. *Science* **277**, 1956–1962 (1997).

[10] Laske, G. & Masters, G. A. A global digital map of sediment thickness. *EOS Trans. Am. Geophys. Union* **78**, F483 (1997).

[11] Jordan, T. H. Composition and development of the continental tectosphere. *Nature* **274**, 544–548 (1978).

[12] Hager, B. H. Subducted slabs and the geoid: Constraints on mantle rheology and flow. *J. Geophys. Res.* **89**, 6003–6015 (1984).

[13] Colli, L., Ghelichkhan, S. & Bunge, H.-P. On the ratio of dynamic topography and gravity anomalies in a dynamic Earth. *Geophys. Res. Lett.* **43**, 2510–2516 (2016).

[14] Yang, T. & Gurnis, M. Dynamic topography, gravity and the role of lateral viscosity variations from inversion of global mantle flow. *Geophys. J. Int.* **207**, 1186–1201 (2016).

[15] Valentine, A. P. & Sambridge, M. Optimal regularisation for a class of linear inverse problem. *Geophys. J. Int.* **215**, 1003–1021 (2018).

[16] Trampert, J. & Snieder, R. Model estimations biased by truncated expansions: Possible artifacts in seismic tomography. *Science* **271**, 1257–1260 (1996).

[17] Yang, T., Moresi, L., Muller, R. D. & Gurnis, M. Oceanic residual topography agrees with mantle flow predictions at long wavelengths. *Geophys. Res. Lett.* **44**, 10896–10906 (2017).

[18] MacKay, D. Bayesian interpolation. *Neural. Comput.* **4**, 415–447 (1992).

[19] Schaeffer, A. J. & Lebedev, S. Global shear speed structure of the upper mantle and transition zone. *Geophys. J. Int.* **194**, 417–449 (2013).
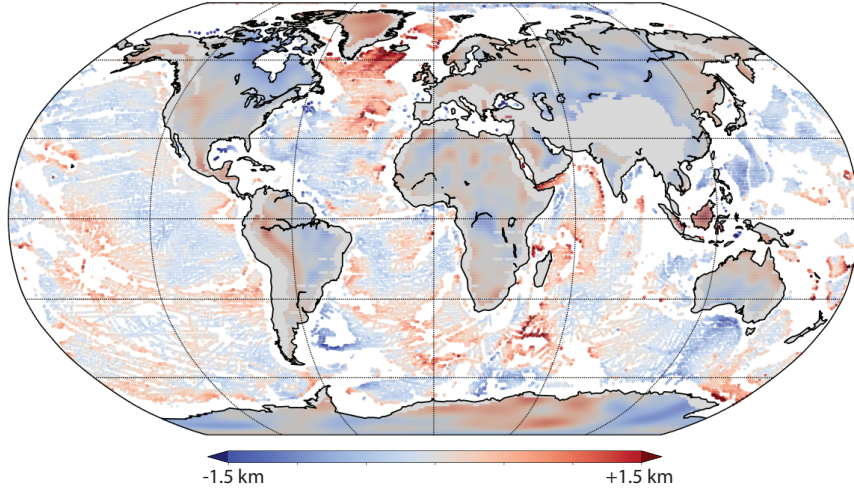
Supplementary Figures

(a) Spot Measurements Only
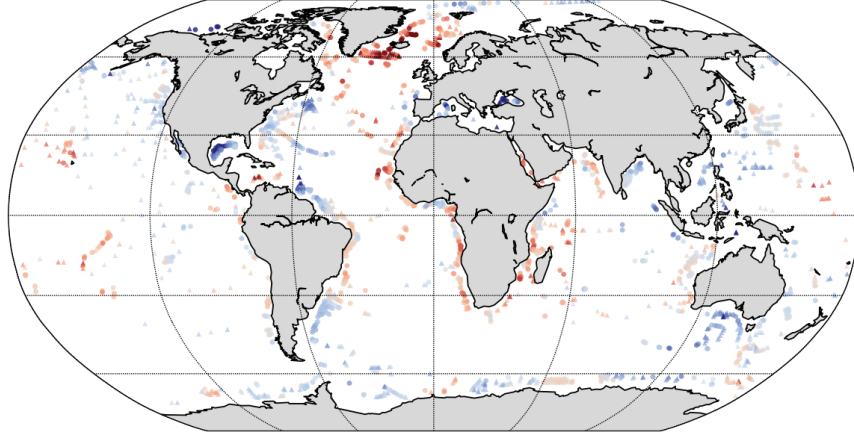
(b) Spot & Ship-Track
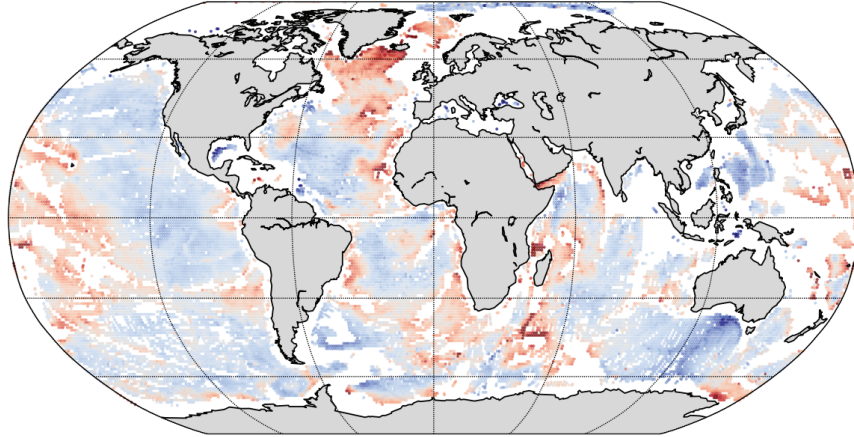
(c) Spot, Ship-Track and Continental (assuming constant admittance)
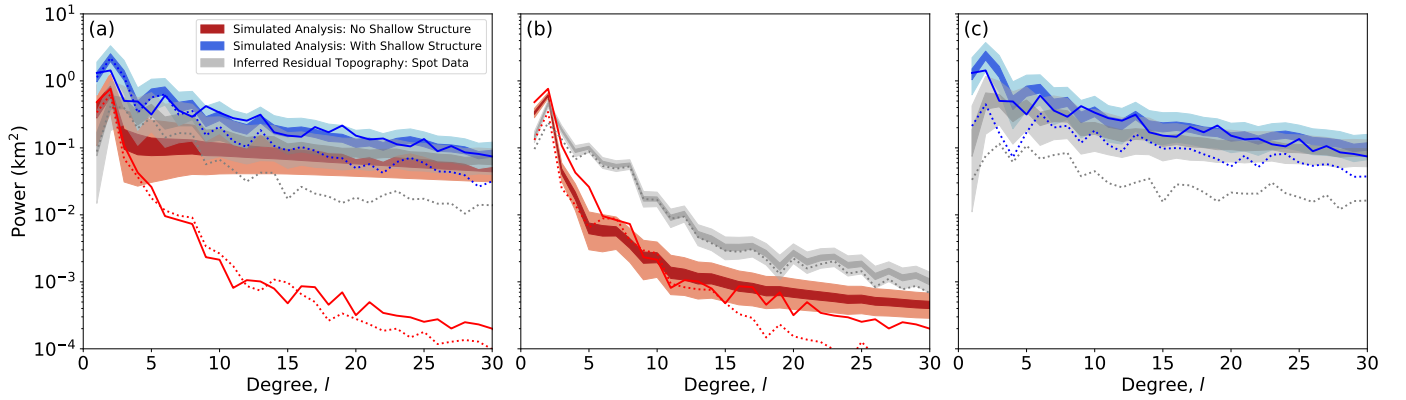

-1.5 km   +1.5 km

Supplementary Figure 1: **Observational Constraints on Residual Topography:** (a) An updated compilation of the point-wise measurements of residual topography from Hoggard *et al.* (2017) [1] (1,160 of these points incorporate a crustal correction – circles – whilst 870 do not – triangles). To generate our global spherical harmonic residual topography estimate, these point-wise constraints were supplemented in the oceans with residual depth estimates from ship-track bathymetry, with this combined dataset illustrated in panel (b). In panel (c), we illustrate the final dataset of Hoggard *et al.* (2016) [5], where a model of residual topography was utilised on continents. This model assumed a constant admittance to transform free-air gravity anomalies to residual topography. In our study, we utilised the residual topography estimates plotted in panel (b) only.
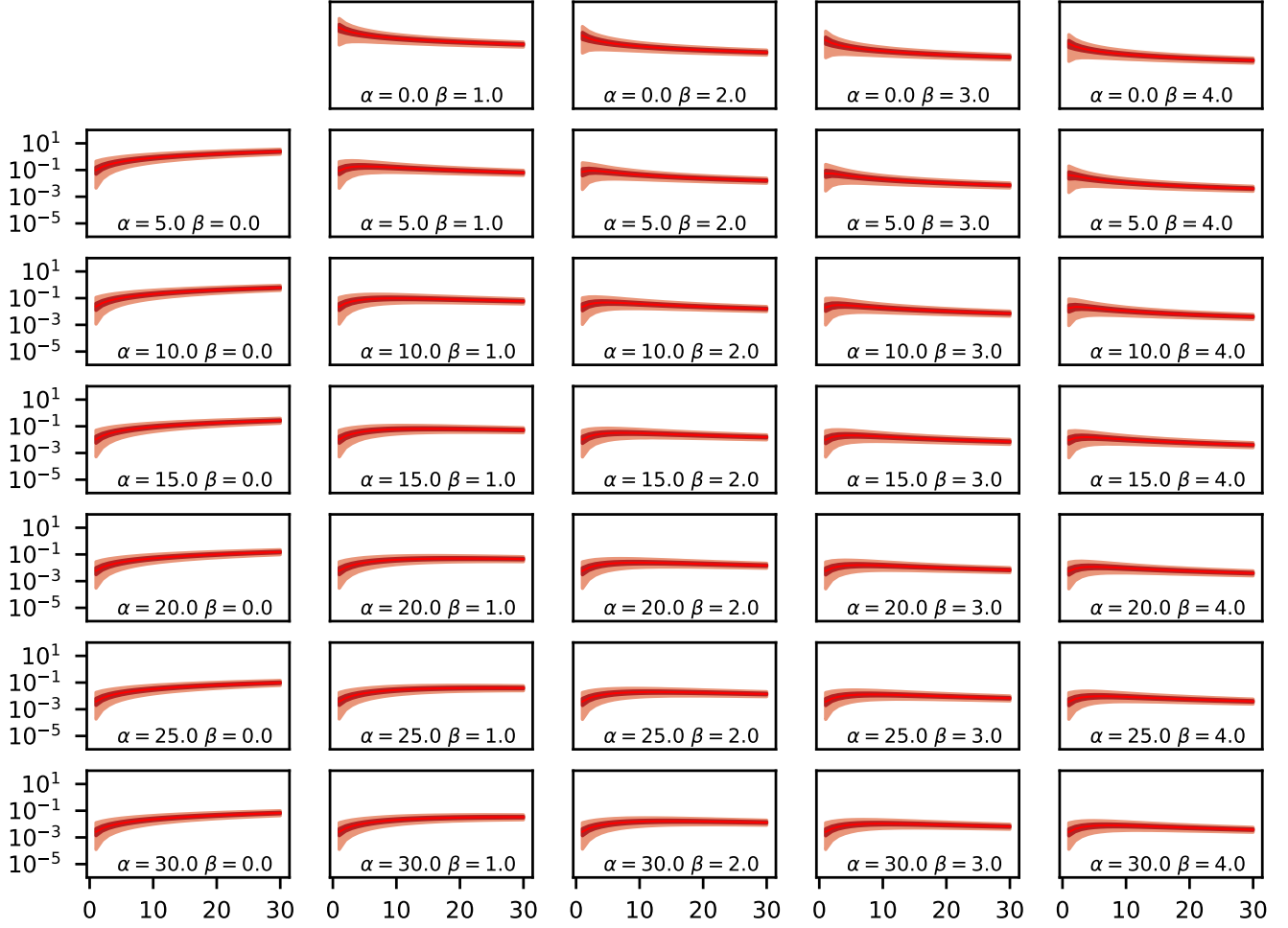
Supplementary Figure 2: **Prior assumptions encoded within the Tikhonov-style regularisation approach adopted by [5]**. Shaded regions represent 50% and 99% confidence intervals encompassed by 10^6 samples from the prior distribution represented by $\mathbf{C_m^{-1}} = \alpha^2\mathbf{I} + \beta^2\mathbf{H}$, for a range of values of α and β. Note that [5] chose $\alpha = 20$ and $\beta = 1.0$, with ranges of 10–32 and 0.56–1.78, respectively.
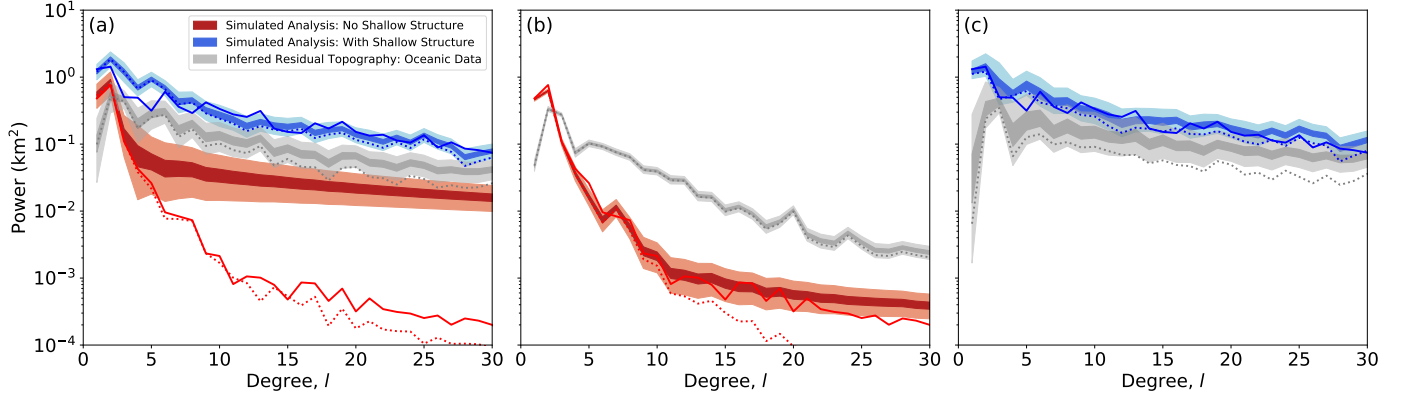
Supplementary Figure 3: **Power spectra obtained from simulated datasets and observational constraints using Tikhonov-style inversions similar to [5] (oceanic point-wise and ship-track locations)**: in all plots, solid lines denote results from (simulated) datasets with complete, high-density global coverage; dashed lines represent results obtained using data only at the point-wise and ship-track observation points (illustrated in Supplementary Fig. 1b). Shaded regions represent 50% and 99% confidence intervals, defined as described in Methods. Red colours denote inversions of a simulated dataset with no shallow structure; blue colours depict a simulated dataset with shallow structures present. Grey colours represent results obtained from the observational constraints. In (a), regularisation parameters have been determined automatically by applying the method of [15] to the observational constraints, and using this choice on all other datasets. In (b), the regularisation parameters are determined from one simulation (without shallow structure; full global coverage), while in (c) they are determined from the other (with shallow structure; full global coverage). The observational constraints clearly share spectral characteristics with the simulation that contains shallow structure.

Supplementary Figure 4: **Power spectra obtained from simulated datasets and observational constraints using Tikhonov-style inversions similar to [5] (oceanic point-wise locations only)**: as in Supplementary Fig. 3, but for the point-wise/spot observational constraints only (illustrated in Supplementary Fig. 1a).
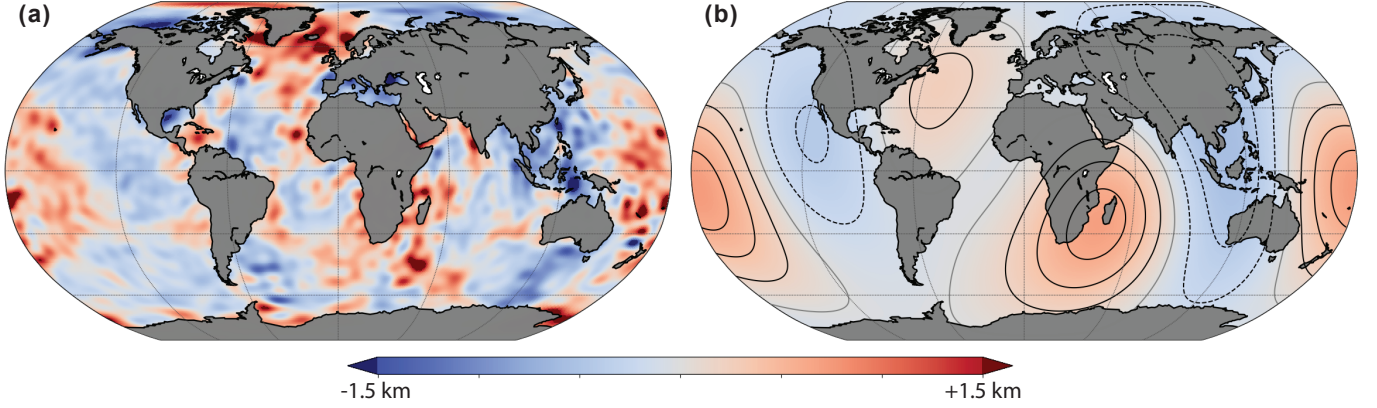
Supplementary Figure 5: Inferred Oceanic Residual Topography: spherical harmonic model (regularised using ARD) up to $l = 30$, of our updated compilation of oceanic (point-wise and ship-track) residual topography measurements (displayed in Supplementary Fig. 1b). In panel (b) we display the $l = 0 - 3$ components of this model, which is the mean model of the distribution plotted in Fig. 2 of the main manuscript. Contours are at 0.2 km intervals, with dashed contours denoting negative values and grey indicating the zero contour. For the $l = 0 - 3$ components of this mean model, amplitudes range from -0.59 km to 0.76 km. Peak amplitudes at $l = 0 - 3$, across the entire distribution of models, are $\sim 0.8 \pm 0.1$ km.
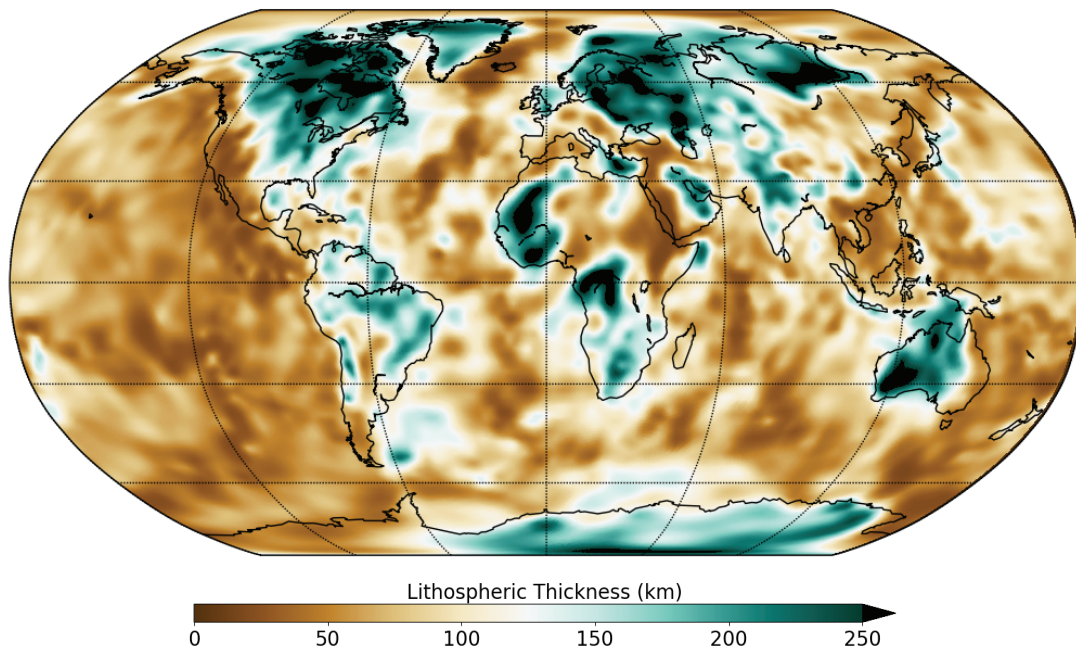
Supplementary Figure 6: **Lithospheric thickness estimate used in this study:** Derived from the SL2013sv tomography model of Schaeffer and Lebedev (2013) [19] (see Methods for further information).

(a) Synthetic Residual Topography (All Components)　　**(b) Synthetic Dynamic Topography (Flow-Related Component)**

-1.5 km　　+1.5 km

Supplementary Figure 7: **Residual vs. dynamic synthetic topography predictions from our model incorporating shallow structure:** in (a) the synthetic topography field includes both isostatic contributions from lithospheric thickness variations and mantle flow-related contributions. If we assume that these lithospheric thickness variations are purely thermal in origin, are not taking part in convection and make an isostatic contribution to the synthetic residual topography field, their effect can be subtracted out to isolate the dynamic (flow-related) component of residual topography, which is illustrated in panel (b).
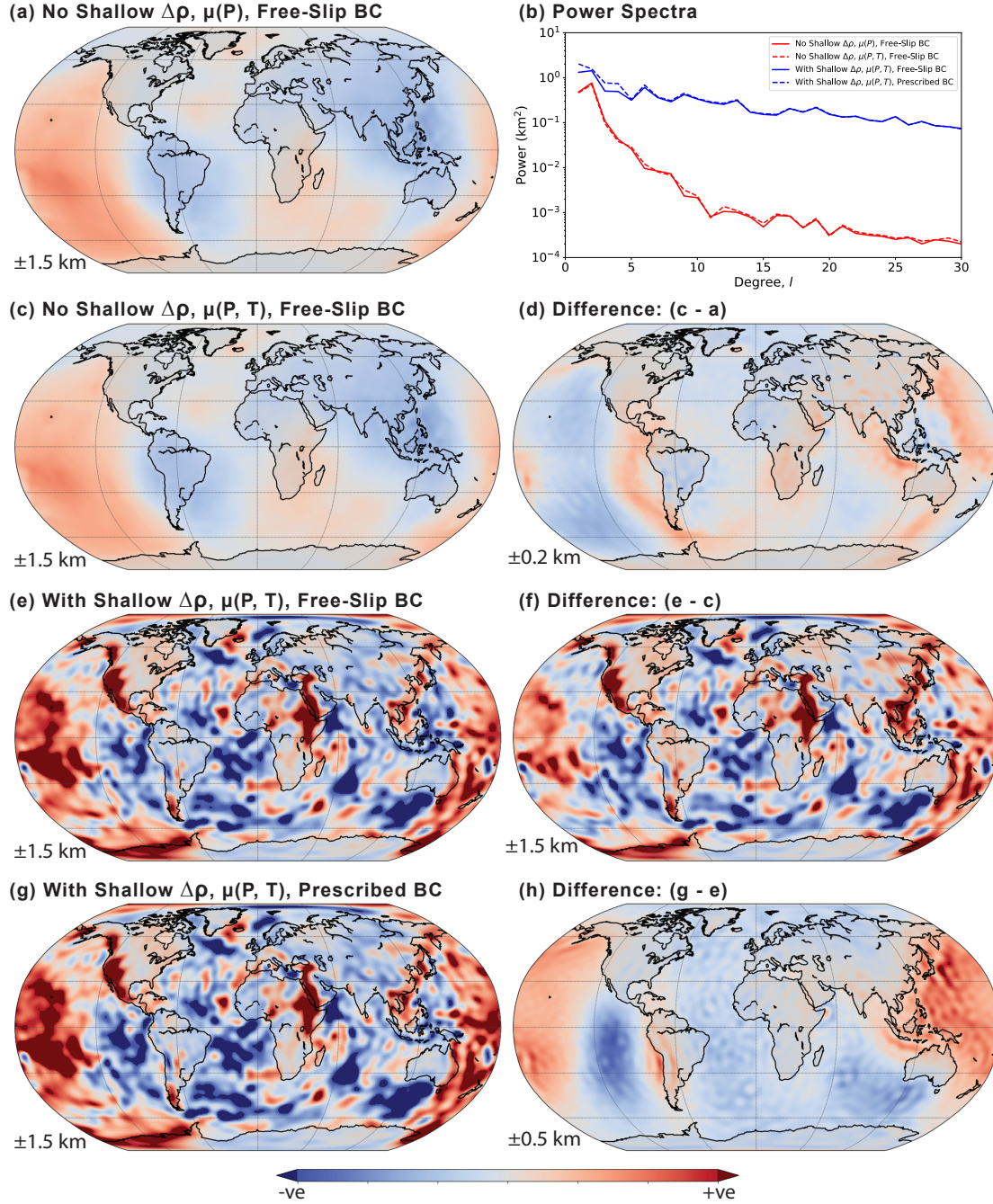
Supplementary Figure 8: **Viscosity profiles for the models examined herein:** (a) the depth-dependent viscosity profile utilised in our model that neglects shallow mantle structure; (b) the minimum, mean and maximum viscosities at any given depth from our models that account for shallow structure, where viscosity is a function of depth and temperature.

(a) No Shallow △ρ, μ(P), Free-Slip BC

±1.5 km

(b) Power Spectra

(c) No Shallow △ρ, μ(P, T), Free-Slip BC

±1.5 km

(d) Difference: (c - a)

±0.2 km

(e) With Shallow △ρ, μ(P, T), Free-Slip BC

±1.5 km

(f) Difference: (e - c)

±1.5 km

(g) With Shallow △ρ, μ(P, T), Prescribed BC

±1.5 km

(h) Difference: (g - e)

±0.5 km

-ve   +ve

Supplementary Figure 9: **Simulated topography from a range of geodynamical models:** (a) synthetic topography from a model that neglects mantle density and viscosity heterogeneity above 300 km depth; (c) as in panel a, but incorporating a temperature and pressure dependent viscosity, as illustrated in Supplementary Fig. 8, with panel (d) highlighting the difference between these cases. In panel (e), the model incorporating shallow (density and viscosity) heterogeneity is illustrated, with the difference to c highlighted in Panel (f). Panel (g), shows a case with a prescribed kinematic surface boundary condition [8], as opposed to the free-slip boundary condition, with the difference to e highlighted in Panel (h). Panel (b) displays the spectral decomposition from all cases. Note that these spectra are unregularised and do not account for sampling biases associated with the observational constraints. Numeric values for each panel indicate colour bar bounds.